

An Electromagnetically Driven Micromirror with a Large Stroke

Chuan-Hui Ou,¹ Nguyen Van Toan,^{1*} and Takahito Ono^{1,2**}

¹Department of Mechanical Systems Engineering, Tohoku University,
6-6-01 Aramaki-Aza-Aoba, Aoba-ku, Sendai 980-8579, Japan

²Micro System Integration Center, Tohoku University,
519-1176 Aramaki-Aza-Aoba, Aoba-ku, Sendai 980-0845, Japan

(Received February 21, 2024; accepted April 19, 2024)

Keywords: electromagnetic force, micromirror, interferometer, microfabrication, large stroke

In this research, a micromirror driven by electromagnetic force is designed and fabricated. The micromirror features a microfabricated L-shaped spring for large deflection and a bulk permanent magnet with a size of $1 \times 1 \times 1.5 \text{ mm}^3$ mounted on the micromirror for generating electromagnetic actuation force. The device has a footprint of approximately $10 \times 10 \text{ mm}^2$. The design of the micromirror is based on Castigliano's theorem, theoretic spring constant evaluation, and finite element analysis, which are applied to estimate the deflection. The fabricated micromirror can be actuated at the resonance frequency in the atmosphere. The piston vibration at a fundamental frequency of 26.6 Hz is desirable for Michelson interferometers. An $830 \text{ }\mu\text{m}$ stroke is achieved by applying 1 Vpp at the resonance frequency, and a 4.44° tilting angle is observed. Overall, the large stroke of the fabricated micromirror implies that the electromagnetic micromirror is promising for high-resolution interferometer applications.

1. Introduction

Miniaturized interferometers have attracted the interest of many researchers for their potential to be intelligent systems-on-a-chip.⁽¹⁾ Miniaturized interferometers can be applied in various fields such as space research, environment monitoring, physical observation, and industrial safety analysis.^(2–5) Compared with conventional interferometers, microfabricated interferometers are compact and cost-effective, which expands their application fields. There are various applications, for instance, Fourier transform infrared spectroscopy (FTIR) for identifying and quantifying chemical compounds and structures,^(6–8) optical coherence tomography (OCT) for medical examination,^(9,10) and hyperspectral imagers for measuring the spectral content of each pixel.^(11,12)

Interferometers generate interferograms by shifting the phase of light. Movable mirrors play an important role in controlling the phase of light in various interferometers. The stroke of a movable mirror directly affects the resolution of interferograms. The long stroke motion is the key factor in attaining a high performance. For gas sensing applications with FTIR, a resolution

*Corresponding author: e-mail: nguyen.van.toan.c6@tohoku.ac.jp

**Corresponding author: e-mail: takahito.ono.d4@tohoku.ac.jp

<https://doi.org/10.18494/SAM5027>

of 8 cm^{-1} is required for straight-chain alkanes such as methane and ethane.⁽¹³⁾ To achieve the resolution of 8 cm^{-1} , the stroke of the micromirror should be larger than $625\text{ }\mu\text{m}$.

Several translational micromirrors, which are mainly driven by electrostatic,⁽¹⁴⁾ piezoelectric,⁽¹⁵⁾ thermoelectric,⁽¹⁶⁾ or electromagnetic actuation,⁽¹⁷⁾ have been proposed. Generally, piezoelectric and electrostatic micromirrors are precisely controlled, but they have limited strokes. Thermoelectric micromirrors exhibit large strokes of around several hundred micrometers to one millimeter; however, they are sensitive to ambient temperature and have a longer response time because the heating and cooling processes are needed. In contrast, the electromagnetic actuation method has neither sensitivity to environmental temperature nor the problem of long response time. However, most electromagnetic micromirrors have strokes below $300\text{ }\mu\text{m}$.

Each type of micromirror faces its own challenges that may significantly affect its application performance. Thus far, a device that addresses all the issues has not yet been developed. Electromagnetic micromirrors are promising candidate solutions because of the high diversity of actuation materials and designs. The major issue of electromagnetic micromirrors is the limited stroke. Stroke can be improved in various ways, for instance, by adjusting the structural design or changing the actuation material.

The springs of most electromagnetic micromirrors have low spring constants under bending with one free end. However, the spring constant varies with the boundary condition. In piston motion, the boundary condition of a spring can be seen as a guided end, which means that the in-plane movement of the end of the spring is constrained. The spring constant under the guided end boundary condition might be totally different from that under the free end boundary condition. Many spring designs focus on reducing the spring constant under the free end boundary condition instead of the guided end boundary condition. Consequently, under the nonoptimized spring constant with a limited actuation force, the stroke is limited. As for actuation, electromagnetic force depends on the volume of magnetic material and the current in the coil. Most electromagnetic micromirrors use a magnetic film, micromagnet, or embedded coil, which can only provide a limited magnetic force.

We present an electromagnetic micromirror with a large stroke by applying L-shaped springs and a bulk permanent magnet. The combination of optimized microsprings and a permanent micromagnet led to a breakthrough in the stroke of electromagnetic micromirrors. The springs were optimized to achieve an extremely low spring constant and a low stress concentration by introducing the L-shaped structure. With the optimized springs, the micromirror can realize a large displacement without fracture. The bulk permanent magnet can provide a large actuation force owing to its size and the high remanent magnetization. Theoretical design, finite element analysis, device fabrication, and evaluation are performed in this research.

2. Design of Micromirror

A schematic of the proposed electromagnetic micromirror is shown in Fig. 1. The mirror plate is suspended by L-shaped springs, and a permanent magnet is mounted on the mirror plate. An actuation coil is placed under the micromirror device for electromagnetic actuation. When

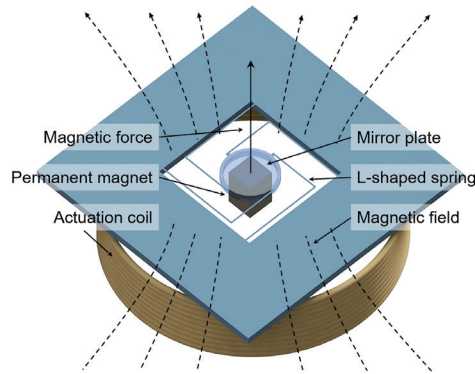


Fig. 1. (Color online) Schematic of electromagnetic micromirror with actuation coil.

current flows into the actuation coil, the micromirror device will be actuated in the vertical direction. L-shaped springs are introduced to reduce the spring constant of the system and the tension of the springs for larger strokes.

The dimensions of the L-shaped springs are determined from the calculation of the deflection of the spring with one free end, as shown in Fig. 2. Each L-shaped spring is divided into segments A and B with lengths a and b , respectively. Point C is a free end and point D is fixed. Force P is applied at C. In Castigliano's theorem, the partial derivative of energy with force gives the displacement. The strain energy U stored in an L-shaped spring can be expressed as

$$U = \int_0^a \frac{(Px)^2}{2EI} dx + \int_0^b \frac{(Pa)^2}{2GJ} dx + \int_0^b \frac{(Px)^2}{2EI} dx, \quad (1)$$

where E is Young's modulus, I is the area moment of inertia, G is the shear modulus, and J is the torsion constant. The vertical displacement u_c at point C is given by

$$u_c = \frac{\partial U}{\partial P}. \quad (2)$$

The device was designed to have a mirror plate radius of 1 mm and a size of $10 \times 10 \text{ mm}^2$. According to Castigliano's theorem, the spring length and thickness have higher effects on the displacement than the spring width. A longer and thinner spring will have a higher performance. To ensure robustness, the thickness of the springs should be sufficiently large. Therefore, the priority task is to increase the length of the springs as much as possible and determine a moderate spring thickness. Finally, the optimal dimensions of the springs in a $10 \times 10 \text{ mm}^2$ device were determined to be $7 \text{ }\mu\text{m}$ in thickness and $50 \text{ }\mu\text{m}$ in width with a 2 mm length of segment A and a 3.2 mm length of segment B. The equivalent bending spring constant of a single L-shaped spring under the free end boundary condition, k_e , was roughly estimated to be 0.0174 using

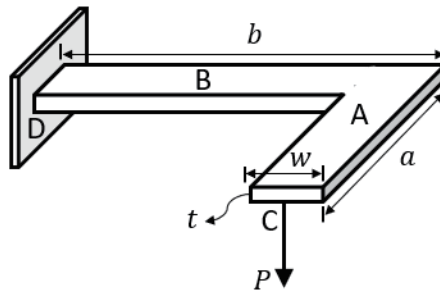


Fig. 2. Model of L-shaped spring.

$$\frac{1}{k_e} = \frac{1}{k_a} + \frac{1}{k_b}, \quad (3)$$

where k_a and k_b are the spring constants of segments A and B shown in Fig. 2, respectively, which are expressed as

$$k_a = \frac{3EI_a}{a^3}, \quad (4)$$

$$k_b = \frac{3EI_b}{b^3}. \quad (5)$$

Here, E is Young's modulus and I_a and I_b are the moments of inertia of segments A and B, respectively, with $I_a = I_b = wt^3/12$.

The parameters used in the estimation are summarized in Table 1. After deciding the parameters of the L-shaped spring and verifying that it was possible for a single L-shaped spring to achieve a low spring constant under the fixed-free end boundary condition, the spring constant of the entire system was estimated and compared with those of other types of springs.

The most common microspring shapes are straight beam, crab-leg, folded, and serpentine. Figure 3 shows the schematic of each spring shape, and Table 2 summarizes the spring constant formulas of different spring shapes in out-of-plane directions. Since the spring elements of the L-shaped spring are similar to those of the crab-leg spring, the spring constant of the L-shaped spring was estimated using the same formula as for the crab-leg spring. The differences between the crab-leg and L-shaped springs are in the anchor position and effective spring length in a limited space.

To find the most optimal spring shape for the micromirror, the spring constants were estimated using the parameters in Table 3. The full size of the mechanical element was limited to within $4 \times 4 \text{ mm}^2$, the size of the mirror plate, $m \times m$, was set as $2 \times 2 \text{ mm}^2$, and the width of springs, w , was set as $50 \text{ }\mu\text{m}$. Under this condition, the L-shaped spring has the lowest spring

Table 1
Parameters for spring constant estimation.

Length of segment A, a	2 mm
Length of segment B, b	3.2 mm
Width, w	50 μm
Thickness, t	7 μm
Area moment of inertia of segments A and B, I_a, I_b	$1.43 \times 10^{-21} \text{ m}^4$
Young's modulus, E	168.9 GPa

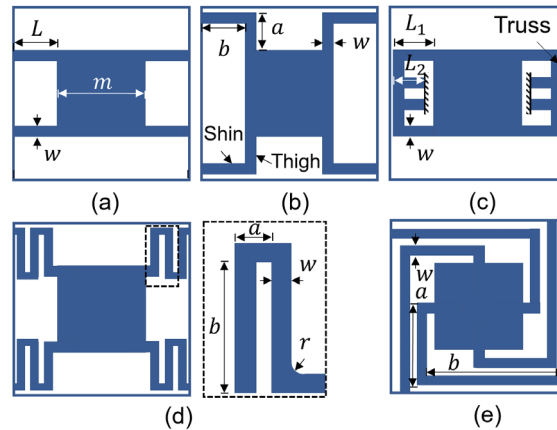


Fig. 3. (Color online) Spring shapes. (a) Straight beam spring. (b) Crab-leg spring. (c) Folded spring. (d) Serpentine spring. (e) L-shaped spring.

Table 2
Summary of spring constant formulas.

Spring	Spring constant formula ⁽¹⁸⁾
Straight beam spring	$k = \frac{48EI}{L^3}, \tag{1}$ <p>where E is Young's modulus, I is the area moment of inertia $I = wt^3/12$, and t is the thickness.</p>
Crab-leg spring	$k = \frac{48S_{ea}S_{eb}(S_{gb}a + S_{ea}b)(S_{eb}a + S_{ga}b)}{S_{eb}^2S_{gb}a^5 + 4S_{ea}S_{eb}^2a^4b + S_{eb}S_{ga}S_{gb}a^4b + 4S_{ea}S_{eb}S_{ga}a^3b^2 + 4S_{ea}S_{eb}S_{gb}a^2b^3 + 4S_{ea}^2S_{eb}ab^4 + S_{ea}S_{ga}S_{gb}ab^4 + S_{ea}^2S_{ga}b^5}, \tag{2}$ <p>where $S_{ea} \equiv EI_a$, $S_{eb} \equiv EI_b$, $S_{ga} \equiv GJ_a$, $S_{gb} \equiv GJ_b$, I_a and I_b are the moments of inertia of the thigh and shin, respectively, G is the shear modulus $G = E/2(1 + \nu)$ and ν is Poisson's ratio. Moreover, J_a and J_b are the torsion constants of the thigh and shin, respectively, $J = \beta wt^3$, and β is a factor for the rectangular section, which is about 0.3 when $w/t = 7.1$.</p>
Folded spring	$k = \frac{24EI}{L^3} \tag{3}$ <p>when $L_1 = L_2 = L$ and for stiff truss.</p>
Serpentine spring	$k = \frac{48S_{ea}S_{eb}S_{ga}S_{gb}}{S_{eb}S_{ga}a^2(S_{gb}a + S_{ea}b)n^3 - 3S_{ea}S_{eb}S_{ga}a^2bn^2 + S_{ea}b(2S_{eb}S_{ga}a^2 + 3S_{eb}S_{gb}ab + S_{ga}S_{gb}b^2)n - S_{ea}S_{ga}S_{gb}b^3}, \tag{4}$ <p>where $S_{ea} \equiv EI_a$, $S_{eb} \equiv EI_b$, $S_{ga} \equiv GJ_a$, $S_{gb} \equiv GJ_b$, and n is the number of meanders.</p>
L-shaped spring	Eq. (2)

Table 3
Parameters used in spring constant estimation.

Common parameters			
Mirror plate size, $m \times m$	$2 \times 2 \text{ mm}^2$	Width, w	$50 \text{ }\mu\text{m}$
Thickness t	$7 \text{ }\mu\text{m}$	Young's modulus, E	168.9 GPa
Area moment of inertia, $I_a = I_b = I$	$1.43 \times 10^{-21} \text{ m}^4$	Poisson's ratio, ν	0.262
Shear modulus G	$6.54 \times 10^{10} \text{ Pa}$	Torsion constant, $J_a = J_b = J$	$5.15 \times 10^{-21} \text{ m}^4$
	Parameters	Spring constant (N/m)	
Straight beam spring	$L = 0.9 \text{ mm}$	15.894	
Crab-leg spring	$a = 0.9 \text{ mm}, b = 1 \text{ mm}$	3.011	
Folded spring	$L = 0.9 \text{ mm}$	7.947	
	$a = 0.166 \text{ mm}, b = 1.75 \text{ mm}, n = 6$	0.302	
Serpentine spring	$a = 0.125 \text{ mm}, b = 1.75 \text{ mm}, n = 8$	0.225	
	$a = 0.1 \text{ mm}, b = 1.75 \text{ mm}, n = 10$	0.180	
	$a = 0.083 \text{ mm}, b = 1.75 \text{ mm}, n = 12$	0.149	
L-shaped spring	$a = 2 \text{ mm}, b = 3.2 \text{ mm}$	0.139	

constant. Even though the spring constant of the serpentine spring can be reduced by increasing the number of meanders, there is a limitation when the number of meanders is large. In Table 3, we can also observe that the rate of decrease in the spring constant of the serpentine spring decreases with increasing number of meanders. In addition, the increasing number of meanders in a limited space also limits the fillet radius r , as seen in Fig. 3(d). The fillet radius is important in reducing the stress concentration and improving the fatigue life. Therefore, the L-shaped spring is the most suitable structure for designing micromirrors because it has a high fatigue life and a low spring constant, providing enough fillet radius to reduce the stress concentration.

In the actual design, all the corners are filleted with a radius of $30 \text{ }\mu\text{m}$ to reduce the stress concentration. Finite element analysis (FEA) is applied to predict the deflection and stress distribution precisely at the device level, as shown in Fig. 4. Parameters for the simulation are listed in Table 1. The results show that the vertical displacement is $842 \text{ }\mu\text{m}$ and the maximum stress is 0.283 GPa , which is lower than the strength of single crystal silicon (SCS) specimens. It has been reported that the strength of SCS specimens ranges from 0.31 to 17.5 GPa .⁽¹⁹⁾ To actuate the micromirror, a $1 \times 1 \times 1.5 \text{ mm}^3$ neodymium permanent magnet with a weight of 0.01 g is mounted on the mirror plate. The micromirror can be actuated at resonance. The eigenfrequencies and vibration mode of the micromirror bounded with the permanent magnet are simulated. As shown in Fig. 5, the fundamental frequency with linear out-of-plane motion is 18.8 Hz , which is applicable to interferometer applications. Figure 5 also shows other resonance frequencies and vibration modes, including out-of-plane and in-plane rotations.

A vertical magnetic force F_z generated with a field from an actuation coil and a permanent magnet can be expressed as

$$F_z = M_z \int \frac{d}{d_z} H_z dV, \quad (6)$$

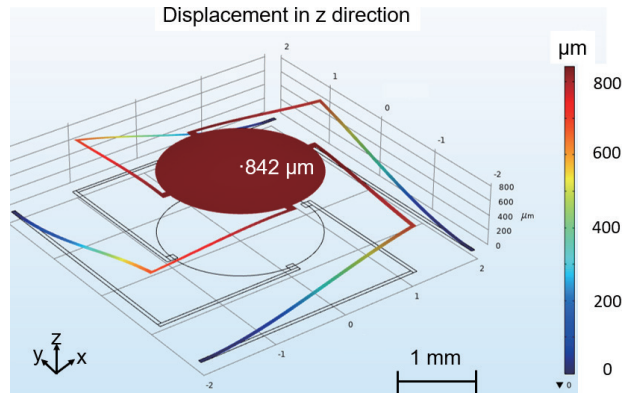


Fig. 4. (Color online) Simulation of micromirror deflection.

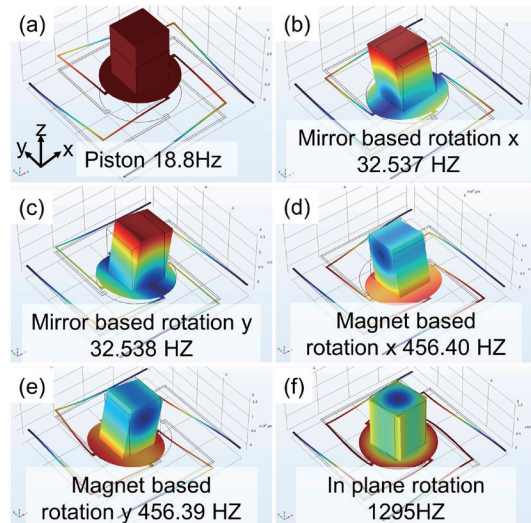


Fig. 5. (Color online) Simulation of eigenfrequencies and vibration mode. (a) Linear motion mode along z -axis. (b) Rotation mode along x -direction with rotation axis on mirror plate. (c) Rotation mode along y -direction with rotation axis on mirror plate. (d) Rotation mode along x direction with rotation axis on top of magnet. (e) Rotation mode along y -direction with rotation axis on top of magnet. (f) Rotation mode along z -axis.

where M_z is the magnetization of the magnet, H_z is the vertical component of the magnetic field generated by the coil, and V is the volume of the magnet. H_z generated by the coil with finite length can be expressed as

$$H_z = \frac{Ni}{2} \left[\frac{z + \frac{L}{2}}{\sqrt{R^2 + \left(z + \frac{L}{2}\right)^2}} - \frac{z - \frac{L}{2}}{\sqrt{R^2 + \left(z - \frac{L}{2}\right)^2}} \right] \hat{z}, \tag{7}$$

where N is the number of turns of the coil, i is the current, and R and L are the radius and length of the coil, respectively. To generate a sufficient actuation force, according to Eqs. (4) and (5), it is important to increase the volume of the permanent magnet, the number of turns of the coil, and the current flowing through the coil.

3. Fabrication of Micromirror

The fabrication process proceeds as follows, starting with a silicon-on-insulator (SOI) wafer with a 7- μm -thick device layer, a 1- μm -thick insulating layer, and a 300- μm -thick handle layer, as shown in Fig. 6(a). A SiO_2 layer is deposited on both sides of the wafer using a plasma-enhanced TEOS chemical vapor deposition (CVD) system, as shown in Fig. 6(b). Next, the SiO_2 layer is patterned by photolithography and etching in a buffered hydrofluoric acid (HF) solution on both sides. Then, the pattern of the mechanical elements is formed on the Si layers by etching from both sides using a deep reactive ion etching (RIE) system [Fig. 6(c)]. The microstructures are released by etching the SiO_2 layer in the buffered HF solution [Fig. 6(d)]. Finally, a neodymium permanent magnet is mounted on the micromirror with conductive glue [Fig. 6(e)]. Figure 7 shows the fabricated micromirror.

Since the bulk permanent magnet is attached with adhesive to the mirror plate consisting of the device layer of the SOI wafer, the mirror surface may be deformed as a result of curing shrinkage. Leaving part of the handling layer under the micromirror plate and applying the adhesive only to the handling layer portion are possible solutions to the flatness problem. In this paper, we demonstrate the prototype of the micromirror; the reflective layer will be added in a future process. The roughness of the mirror surface should be smaller than one-twentieth of the wavelength. For mid-IR applications, a roughness of less than 150 nm is required. Most of the common reflective coating materials used in microfabrication meet this requirement.

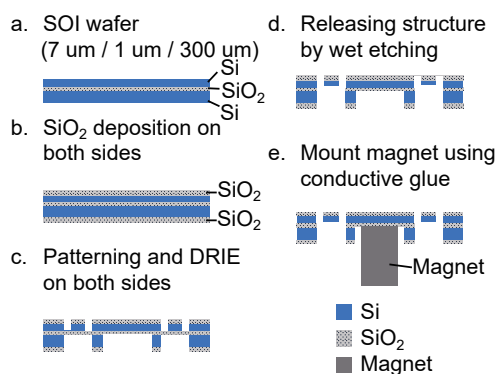


Fig. 6. (Color online) Fabrication process of micromirror.

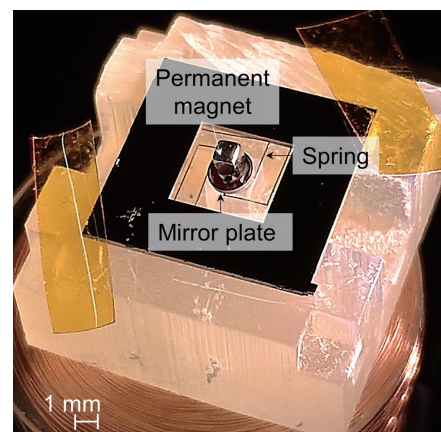


Fig. 7. (Color online) Fabricated micromirror.

4. Experimental Results and Discussion

The displacement and tilting angle of the fabricated micromirror were evaluated with the measurement setup shown in Fig. 8. An alternating current was supplied to the actuation coil with 900 turns of copper wire, 8.5 mm inner diameter, 13 mm outer diameter, 10 mm height, and 0.01 mm wire diameter to actuate the micromirror. The resistance of the coil was 57.5Ω and the inductance was estimated to be 0.008 H using an impedance analyzer. Using a rotating motor with a turn counter, the coil was made by winding a copper wire around a plastic core. The coil had a trade-off relationship between the frequency characteristics and the generated magnetic field. Increasing the number of turns generates a large magnetic field, but because the inductance is large, the output decreases at higher operating frequencies. A limited bandwidth of operation frequency is not favorable for evaluating the micromirror in a wide dynamic range. To ensure the ability of the coil, the frequency response of the produced magnetic field was measured with a gaussmeter. An alternating current of 43 mA was applied to the coil during the measurement. As shown in Fig. 9, there was no significant drop of the magnetic field until 350 Hz, which is sufficient for the actuation frequency at the simulated mechanical resonance of the micromirror of around 19 Hz.

The micromirror motion was recorded using a stroboscopic camera. The frequency of the light flashes from the stroboscope was adjusted to be slightly different from the actuation frequency in order to capture the motion.

The micromirror was actuated by applying alternating current from 0 to 1 V_{pp} and ± 8.7 mA at 26.6 Hz, which is close to the simulation result of 18.8 Hz. The motion of the micromirror was captured for displacement and tilting angle measurements, as shown in Fig. 10. The displacement and tilting angle recorded at two positions are shown in Fig. 11. In the actuation voltage range of 0.15 to 1 V_{pp}, the displacements as well as the tilting angles are positively correlated to the applied voltage. The largest displacement is 830 μm at 1 V_{pp}. The maximum tilting angles at the highest and lowest positions reached 4.4 and -3.1° , respectively.

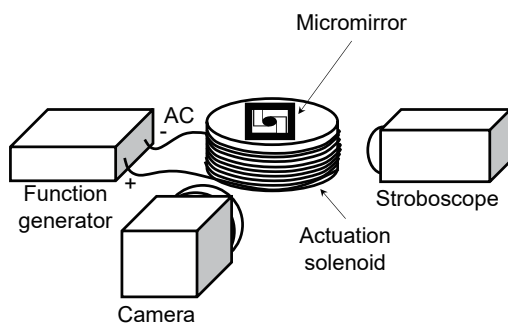


Fig. 8. Setup for measuring displacement and tilting angle.

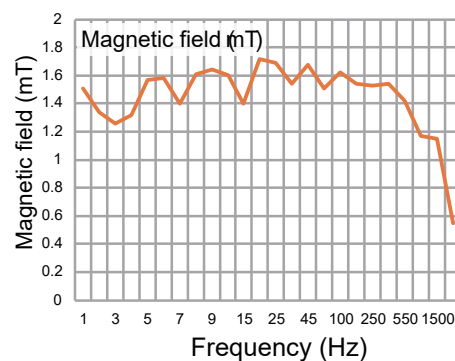


Fig. 9. (Color online) Frequency response of magnetic field.

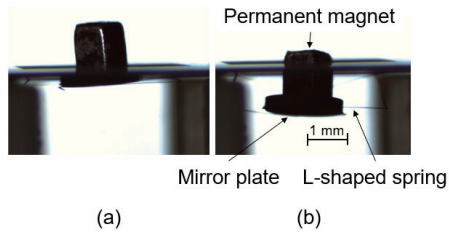


Fig. 10. (Color online) Captured pictures of micromirror motion at (a) highest and (b) lowest positions.

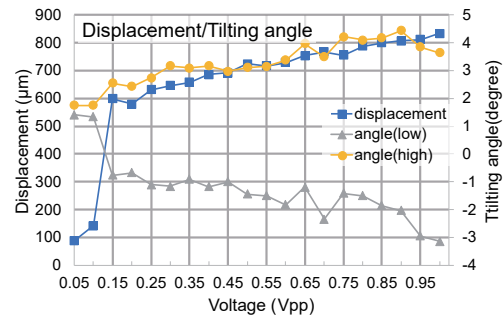


Fig. 11. (Color online) Frequency response of displacement and tilting angle of the micromirror at different magnetic field strengths.

The obtained stroke of the mirror reaches the highest level among the reported electromagnetic micromirrors for interferometer applications. Furthermore, the magnitude of the stroke is similar to that of electrothermally actuated micromirrors, which usually have the largest stroke among all types of micromirrors. Compared with the electrothermally actuated micromirrors, the micromirror used in this study has a faster response and a lower sensitivity to ambient temperature. The long stroke indicates that the fabricated micromirror has the potential to be used in high-resolution interferometers. For example, an 830 μm stroke corresponds to an optical path difference (OPD) of $\sim 1660 \mu\text{m}$ in a Michelson interferometer, and the theoretical resolution $\Delta\nu$ of a Michelson-interferometer-based FTIR could be 6.0 cm^{-1} , as calculated from

$$\Delta\nu = \frac{1}{\sigma_{\square}}, \quad (8)$$

where σ_{max} is OPD, which is twice the displacement. However, a small tilting angle of the micromirror is required. The unfavorable large tilting angle of the fabricated micromirror is possibly caused by the misalignment of the bulk permanent magnet and the asymmetry of the electromagnetic force.

There are several ways to resolve the tilting issue, such as improving the alignment technique when assembling the magnet and micromirror, using four extra coils to control the tilting angle, and replacing the commercial bulk permanent magnet with a bulk magnet electroplated with the photoresist mold fabricated by photolithography to avoid misalignment.

In addition, in Fig. 11, a large change in displacement can be seen in the range from 0 to 0.15 V. This phenomenon might be caused by any of the following three reasons: autoparametric resonance, air damping, and spring softening or hardening. In the first case, if a system exhibits two or more coupled vibration modes, the displacement will be saturated. In the second case, the displacement may be saturated owing to air damping. With increasing ambient pressure, the difference between the slopes of displacement before and after saturation would increase. In the third case, increasing the displacement shifts the resonance frequency and consequently affects the relationship between actuation force and displacement.

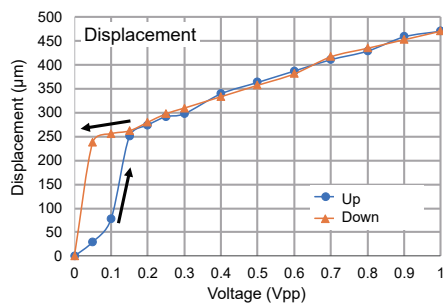


Fig. 12. (Color online) Displacement of micromirror with 100- μm -wide springs measured by voltage ramping up and down.

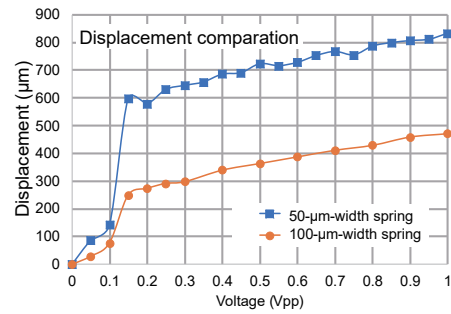


Fig. 13. (Color online) Displacements of micromirrors with springs of different widths.

To discuss the hysteresis and effect of the spring width, the displacement of a micromirror with double-width springs was measured by increasing and decreasing the voltage, as shown in Fig. 12. The behavior observed when increasing the voltage is similar to that in Fig. 11. Both cases showed large displacement changes at 0.15 V. Hysteresis was observed in this experiment. When decreasing the voltage, the slope of the displacement changed little until the actuation voltage approached 0 V. Figure 13 shows the displacements of the micromirrors with different spring widths. The displacement is inversely proportional to the spring width. Both curves also show large displacement changes at 0.15 V.

5. Conclusions

We developed an electromagnetic micromirror that achieved a large stroke of the highest level among electromagnetic micromirrors. The spring constant was optimized with an L-shaped spring to obtain a large stroke, and the use of a bulk permanent magnet improved the actuation force. The spring parameters were optimized for microfabricated devices to withstand macroscale displacement without fracture. The micromirror was driven by the electromagnetic force near the mechanical resonance in the atmosphere. The diameter of the mirror plate was 2 mm, and the footprint of the device was around $10\text{ mm} \times 10\text{ mm}$. The micromirror was capable of moving with a stroke of $\sim 833\text{ }\mu\text{m}$ by applying a voltage of 1 Vpp and a current of 17.4 mA at 26.6 Hz, and the maximum tilting angle was 4.44° . An $833\text{ }\mu\text{m}$ stroke resulted in a $1660\text{ }\mu\text{m}$ optical path difference. With this $1660\text{ }\mu\text{m}$ optical difference, the theoretical resolution for FTIR applications was 6.0 cm^{-1} . The large stroke showed that the electromagnetic micromirrors can potentially improve the resolution in miniature FTIR systems.

Acknowledgments

Part of this work was performed in the Micro/Nanomachining Research Education Center (MNC) and Micro System Integration Center (μSiC) of Tohoku University. This work was supported by JST SPRING, Grant Number JPMJSP2114.

References

- 1 R. F. Wolffenbuttel: IEEE Trans. Instrum. Meas. **53** (2004) 1. <https://doi.org/10.1109/tim.2003.821490>
- 2 G. G. Bentini, M. Bianconi, A. Cerutti, M. Chiarini, G. Pennestri, C. Sada, N. Argiolas, M. Bazzan, and P. Mazzoldi: Opt. Lasers Eng. **45** (2007) 3. <https://doi.org/10.1016/j.optlaseng.2005.05.006>
- 3 A. P. Dean, D. C. Sigee, B. Estrada, and J. K. Pittman: Bioresour. Technol. **101** (2010) 12. <https://doi.org/10.1016/j.biortech.2010.01.065>
- 4 E. Gomez-Ordonez and P. Ruperez: Food Hydrocolloids **25** (2011) 6. <https://doi.org/10.1016/j.foodhyd.2011.02.009>
- 5 Y. Zhao, A. S. Wexler, F. Hase, Y. Pan, and F. M. Mitloehner: J. Environ. Prot. **07** (2016) 12. <https://doi.org/10.4236/jep.2016.712139>
- 6 D. Kowalczyk and M. Pitucha: Materials **12** (2019) 18. <https://doi.org/10.3390/ma12182972>
- 7 Y. M. Eltagoury, Y. M. Sabry, and D. A. Khalil: Adv. Mater. Technol. **4** (2019) 10. <https://doi.org/10.1002/admt.201900441>
- 8 Y. M. Sabry, D. Khalil, and T. Bourouina: Laser Photonics Rev. **9** (2015) 1. <https://doi.org/10.1002/lpor.201400069>
- 9 H. Omran, Y. M. Sabry, M. Sadek, K. Hassan, M. Y. Shalaby, and D. Khalil: IEEE Photonics Technol. Lett. **26** (2014) 1. <https://doi.org/10.1109/lpt.2013.2288016>
- 10 J. Singh, J. H. S. Teo, Y. Xu, C. S. Premachandran, N. Chen, R. Kotlanka, M. Olivo, and C. J. R. Sheppard: J. Micromech. Microeng. **18** (2008) 2. <https://doi.org/10.1088/0960-1317/18/2/025001>
- 11 H. Saari, V.-V. Aallos, A. Akujärvi, T. Antila, C. Holmlund, U. Kantojarvi, J. Mäkynen, and J. Ollila: Proc. SPIE **7474** (2009) 74741M. <https://doi.org/10.1117/12.830284>
- 12 H. F. Mao, D. K. Tripathi, Y. Ren, K. K. M. B. D. Silva, M. Martyniuk, J. Antoszewski, J. Bumgarner, J. M. Dell, and L. Faraone: IEEE J. Sel. Top. Quantum Electron. **23** (2017) 2. <https://doi.org/10.1109/jstqe.2016.2643782>
- 13 B. K. Hart and P. R. Griffiths: Environ. Sci. Technol. **34** (2000) 7. <https://doi.org/10.1021/es9904383>
- 14 D. Lee, U. Krishnamoorthy, K. Yu, and O. Solgaard: Sens. Actuators, A **114** (2004) 2. <https://doi.org/10.1016/j.sna.2003.11.024>
- 15 J. Choi, Z. Qiu, C. H. Rhee, T. Wang, and K. Oldham: J. Micromech. Microeng. **24** (2014) 7.
- 16 H. P. Chen, M. Y. Li, Y. Zhang, H. Xie, C. Chen, Z. Peng, and S. Su: Sensors **18** (2018) 2.
- 17 Y. Xue, H. Zuo, and S. Y. He: J. Micromech. Microeng. **27** (2017) 10. <https://doi.org/10.1088/1361-6439/aa8779>
- 18 G. K. Fedder, Simulation of Microelectromechanical Systems: University of California, Berkeley (1994).
- 19 O. M. Jadaan, N. N. Nemeth, J. Bagdahn, and W. N. Sharpe: J. Mater. Sci. **38** (2003) 20.